Liu *et al. Microstructures* 2024;4:2024048
**DOI:** 10.20517/microstructures.2024.15

**Microstructures**

**Research Article**

**Open Access**

Check for updates

# Synergistic regulation of color and mechanical properties of silicon nitride ceramics via engineering hollow structures of Eu-enriched secondary phases

**Ning Liu[1,2,3], Tengfei Hu[4], Zhengqian Fu[4], Jingxian Zhang[3], Yusen Duan[3], Zhen Wang[1], Fangfang Xu[4], Shaoming Dong[1,3]**

[1]Engineering & Technology Center for Aerospace Materials, Wuzhen Laboratory, Jiaxing 314500, Zhejiang, China.
[2]School of Materials Science and Engineering, Shaanxi Normal University, Xi'an 710119, Shaanxi, China.
[3]Key Laboratory of Advanced Structural Ceramics and Ceramics Matrix Composites, Shanghai Institute of Ceramics, Chinese Academy of Sciences, Shanghai 200050, China.
[4]Analysis and Testing Center for Inorganic Materials, Shanghai Institute of Ceramics, Chinese Academy of Sciences, Shanghai 200050, China.

**Correspondence to:** Dr. Tengfei Hu, Analysis and Testing Center for Inorganic Materials, Shanghai Institute of Ceramics, Chinese Academy of Sciences, 1295 Dingxi Road, Shanghai 200050, China. E-mail: hutf@ucas.ac.cn; Prof. Jingxian Zhang, Key Laboratory of Advanced Structural Ceramics and Ceramics Matrix Composites, Shanghai Institute of Ceramics, Chinese Academy of Sciences, 1295 Dingxi Road, Shanghai 200050, China. E-mail: jxzhang@mail.sic.ac.cn

**How to cite this article:** Liu N, Hu T, Fu Z, Zhang J, Duan Y, Wang Z, Xu F, Dong S. Synergistic regulation of color and mechanical properties of silicon nitride ceramics via engineering hollow structures of Eu-enriched secondary phases. *Microstructures* 2024;4:2024048. https://dx.doi.org/10.20517/microstructures.2024.15

**Received:** 22 Feb 2024 **First Decision:** 14 Jun 2024 **Revised:** 24 Jun 2024 **Accepted:** 26 Jul 2024 **Published:** 9 Aug 2024

**Academic Editors:** Jungho Ryu, Mojca Otoničar, Zibin Chen, Dae-Yong Jeong **Copy Editor:** Fangling Lan **Production Editor:** Fangling Lan

## Abstract

$Si_3N_4$ ceramics, renowned for their superior mechanical properties, are widely regarded as the most promising materials for electronic device casing. This is particularly evident in the context of 5th generation mobile networks, where they outperform both glass and zirconia. However, achieving a synergetic balance between color and mechanical properties remains a significant challenge. In this study, we propose the use of phase separation in liquid phases, supported by a novel $Eu_2O_3$-YAG-MgO system, to engineer hollow structures. This approach aims to achieve high-toughness colored $Si_3N_4$ ceramics. The resulting hollow structure not only acts as a reinforcing phase in response to the stress field caused by lattice mismatch but also serves as one of the dominant chromophores. This is achieved through the 5d→4f transition of $Eu^{2+}$ coupled with the $^5D_0 \rightarrow {}^7F_J$ transition of $Eu^{3+}$ under photon excitation. These findings offer new insights into the development of high-performance $Si_3N_4$ ceramics with well-controlled color.

**Keywords:** $Si_3N_4$ ceramics, Eu ions, hollow structures, optical properties, mechanical properties

## INTRODUCTION

The escalating demand for 5th generation mobile communication technology necessitates the development of enclosure materials for electronic products, including cell phones and smart wearable devices, to satisfy stringent properties standards[1,2]. These include high thermal conductivity (k), with $k > 20$ W/(m·K), for effective equipment cooling; low dielectric loss (tanδ), with $\tan\delta < 10^{-3}$, for optimal signal transmission, high mechanical properties, with fracture toughness ($K_{IC}$) > 10 MPa·$m^{1/2}$ and high flexural strength (σ) > 700 MPa, to ensure sufficient damage tolerance. Such stringent requirements render plastic-based, metal-based and glass-based materials and traditional structure ceramics such as zirconia ($ZrO_2$) and alumina ($Al_2O_3$) unsuitable. Alternatively, silicon nitride ($Si_3N_4$) has emerged as a leading contender for use in 5G electronic products, due to its superior overall performance, as depicted in Supplementary Figure 1. However, the issue of single color (typically grey) coupled with control over mechanical properties remains a significant challenge for large-scale commercialization[3,4]. Therefore, there is an increasing urgency to address both color regulation and improvement of mechanical performance.

In the realm of color regulation, rare earth metal ions ($Re^{3+}$) exhibit the capacity to absorb light in a manner that is triggered by the visible light excitation of a 4f→4f electron transition[5,6]. Notably, among these rare earth metal ions, $Eu^{3+}$ ions have the ability to transmute ultraviolet (UV) radiation into a strong orange-red emission. They are also highly sensitive to their coordination environment due to the unique combination of intra-configurational 4f→4f transitions that are either magnetic or electric-dipole in nature[7,8]. These attributes position $Eu^{3+}$ as a promising candidate for use as a colorant in the creation of orange, red, or similar orange-red $Si_3N_4$ ceramics. However, conventional coloring strategies such as dissolving $Eu^{3+}$ ions within lattices to color ceramics, which has been successfully employed in zirconia[9-11], are not applicable to $Si_3N_4$ coloring. This is primarily due to the robust covalent nature of the Si-N bond in β-$Si_3N_4$[12], coupled with the substantial radius difference between $Si^{4+}$ (0.41 Å[13]) and $Eu^{3+}$ (1.06 Å[14]). In this case, the design of $Eu^{3+}$-doped second crystal phases or new local structures as chromophores is the alternative way. Besides, it is reported that the introduction of second phases or novel local structures can also act as a feasible and practical way for improving mechanical properties[15-17].

The selection of sintering additives in the liquid phase sintering process of $Si_3N_4$ is critically important due to their significant influence on the formation of secondary phases and novel local structures. Compared to the conventional sintering additives [e.g., yttrium oxide-aluminum oxide ($Y_2O_3$-$Al_2O_3$)[18], ytterbium oxide-aluminum oxide ($Yb_2O_3$-$Al_2O_3$)[19], MgO[20], yttrium aluminum garnet (YAG, $Y_3Al_5O_{12}$)[21], *etc.*], we develop YAG-MgO as a sintering additive for its lower eutectic temperature (< 1,613 K[21]) than YAG or MgO via the YAG-MgO-$SiO_2$-$Si_3N_4$ reaction. The lower eutectic temperature offers more time for α-$Si_3N_4$ dissolution in the eutectic liquid phase, and then will promote the growth of high aspect ratio β-$Si_3N_4$ grains[22-24] and the formation of second crystal phases or novel local structures.

In this contribution, we propose using phase separation and crystallization in liquid phases supported by $Eu_2O_3$-YAG-MgO to engineer hollow structures for achieving the color change from yellow to orange-red, while ensuring excellent mechanical properties of $Si_3N_4$. The combined microstructural characterizations of scanning electron microscopy (SEM), high-resolution transmission electron microscopy (HRTEM), scanning transmission electron microscopy (STEM), energy dispersive X-ray spectroscopy (EDS), electron energy loss spectroscopy (EELS) and cathodoluminescence (CL) were utilized to elucidate the crystallographic characteristics and chemical composition of the hollow structures, including morphology, chemical composition, distribution and luminescent characteristic. Based on these characterizations, the formation mechanism of the hollow structure in $Si_3N_4$ ceramics, as well as its impact on their color and mechanical properties, was meticulously analyzed and discussed.

## MATERIALS AND METHOD

### Raw material

All raw materials were utilized in their analytical grade (99+%), with no additional purification required. Commercial α-$Si_3N_4$ powders (SN-E10, O 1.08 wt%, BET 9.64 $m^2/g$, α > 95 wt%) were procured from UBE Industries Ltd, located in Yamaguchi, Japan. Additionally, other chemicals such as $Eu_2O_3$, $Y_2O_3$, $Al_2O_3$, and MgO were acquired from Haoxi Research Nanomaterials, Inc. situated in Shanghai, China.

### Synthesis of YAG ($Y_3Al_5O_{12}$) powders

YAG powders were synthesized by using purity $Y_2O_3$ and $Al_2O_3$ powders via a solid-state reaction method as reported[25,26]. The mole ratio of $Y_2O_3$ to $Al_2O_3$ powders was maintained at 3:5. Following this, the mixed powders were sintered at 1,400 °C for 3 h with the heating rate of 2 °C·$min^{-1}$ in air using a muffle furnace. The resultant powders after sintering were sieved through a 100-mesh screen to spare. The sintered powder was subjected to X-ray diffraction analysis, which revealed the formation of only the YAG phase [Supplementary Figure 2].

### Preparation of colored $Si_3N_4$ ceramic

$Si_3N_4$ Ceramic was prepared by gas pressure sintering using commercial α-$Si_3N_4$ powders as the primary raw materials, MgO powders and as-prepared YAG powders as sintering additives, $Eu_2O_3$ powders as colorants, Polyvinyl Butyral (PVB) as a binder, and $C_2H_5OH$ as a solvent. The mass fractions of YAG and MgO powders were fixed at 4 and 2 wt%, respectively. The quantities of PVB and $C_2H_5OH$ incorporated were 0.8 to 1 wt% and 200 wt% of the total powder, respectively. $Eu_2O_3$ powders, with varying contents of 2, 4, 5, 6, 7, 8, and 9 wt%, were uniformly blended with raw materials and other additives. This mixture was then subjected to a planetary ball mill for a duration of 2 h. The obtained slurry was subsequently dried and subjected to sieving through a 100-mesh screen. The fine powder is inserted into a stainless steel mold (50 mm × 50 mm) and then pre-pressed at 25 MPa using an oil press. Following demolding, the sample is encased in a multi-layer vacuum compression bag to prevent water ingress and subsequently vacuumed. The vacuum bag is then directly placed into the water chamber of the cold isostatic press and subjected to a pressure of 250 MPa for a duration of 90 s. Upon completion of the cold isostatic process, the vacuum bag is removed to extract the sample, which is then immediately subjected to debonding and sintering. $Si_3N_4$ ceramic samples were synthesized by sintering at 1,850 °C, with a heating rate of 3 °C·$min^{-1}$, a holding time of 2 h, and a nitrogen pressure of 0.6 MPa. This process was preceded by the burnout of the binder at 900 °C for 1 h under vacuum.

### Characterization

The bulk densities (ρ) of the sintered samples were ascertained utilizing the Archimedes method, conducted in distilled water. The Vickers hardness (H) was measured using a Vickers microhardness tester (FV-700, Future-Tech, Japan). This measurement was conducted three times on a polished surface, with the load and holding time set at 10 kg and 10 s, respectively. The flexural strength (σ) was determined using a three-point bending test (Model 5566, Instron Co., High Wycombe, UK). This involved a span of 30 mm and a press speed of 0.5 mm/min, utilizing machined rectangle bars (3 mm × 4 mm × 36 mm) with a polished surface. The data from each specimen were averaged across six tests. The fracture toughness ($K_{IC}$) was measured by the single-edge notched beam method (SENB) at room temperature with a crosshead speed of 0.05 mm/min for a span of 24 mm. The thermal diffusivity (λ) was measured using a laser thermal conductivity meter (LFA-457, Netzsch, Germany). The dielectric loss (tanδ) was measured at a frequency of 1 GHz with an impedance meter (E4991B), in accordance with IPC-TM-650 2.5.5.9-1998. This standard stipulates that the specimens should have dimensions of 50 mm × 50 mm × 0.9 mm.

The bulk samples were subjected to phase identification via X-ray diffraction (XRD, D8 Advance, Bruker, Germany). The data collection for the diffraction was conducted within a range of 10°-80° 2θ, employing a scanning step of 10°/min. Prior to examination with SEM (Magellan 400, FEI, USA), the composites were ground using a resin-bonded diamond wheel (SD54R75B1/3) and polished with varying particle sizes (7, 5, 2.5, and 1 μm) of diamond slurry to achieve a surface finish of 0.02 μm. The microstructure of the samples was examined using transmission electron microscopy (TEM, JEM-2100, JEOL, Japan), encompassing STEM and HRTEM. Within the framework of STEM, both compositional and valence state analyses were conducted utilizing EDS and EELS, respectively. The valence state of the Eu element was also documented using X-ray photoelectron spectroscopy (XPS, ESCALAB 250, Thermo Fisher Scientific, USA).

The optical reflectance within the wavelength range of 380 to 750 nm, along with the Commission International del'Eclairage (CIE) chromaticity coordinates, was ascertained utilizing a Spectrophotometer, which was procured from X-rite in USA. Before color measurement, calibration was conducted utilizing the instrument's standard plate, encompassing both white calibration and zero position calibration. The mean values of L*, a*, and b* were computed to denote the chromaticity value of each sample following three surface measurements. This was achieved by positioning the sample in front of the measuring aperture, which has a diameter of 2 mm. Photoluminescence (PL) emission spectra were performed by a fluorescence spectrometer (Hitachi F-4600, Japan). The luminescence position inside the sample was determined by Scanning Electron Microscopy-Cathodoluminescence (SEM-CL, Gemini450, ZEISS). The optical energy gaps, denoted as Eg, were determined using the Wood and Tauc equation[27,28]. This method involved a transformation of diffuse reflectance spectra to estimate the value of Eg:

$$\alpha h\nu = A(h\nu - Eg)^n$$

where α and hν represent the absorption coefficient and photon energy, respectively, A is a constant, Eg denotes the optical band gap, and n takes on values of 1/2 or 2 for direct allowed and indirect allowed transitions, respectively. According to literature[29,30], silicon nitride displays an optical absorption spectrum that is dominated by the indirect absorption process ($n$ = 2).

## RESULTS AND DISCUSSION

During the liquid-phase sintering process of $Si_3N_4$ ceramics, the assembly of Eu ions, attributed to their high field strength and larger radius, leads to the segregation of the glass phase[31]. This phenomenon is depicted in Supplementary Figure 3. The liquid phase, enriched with Eu, encapsulates the pores, thereby forming a hollow structure at the grain boundary. Furthermore, the generation of these hollow structures within β grains transpires during the solution-reprecipitation process[12], which can be divided into two stages: initially, the α to β phase transformation in the liquid phase is facilitated by the homogeneous mixing of sintering additives (YAG-MgO) and colorants ($Eu_2O_3$) between 1,450-1,800 °C; all transformations into β are completed within this stage. Subsequently, the second stage involves the solution of small β grains and their reprecipitation on larger β grains at elevated temperatures (> 1,800 °C), concurrently introducing hollow structures into the larger β grains [Figure 1A]. A more comprehensive depiction of the second step is illustrated in Figure 1B and C. Two or more adjacent, small β grains with identical orientations are susceptible to dissolution, merging, and growth into larger β grains at elevated temperatures. Concurrently, the gas and liquid phases within the grain boundary are compressed into the β grains at the onset of the merger, and then persistently expelled to the grain boundary as the merger progresses. However, when sintering or grain growth is impeded, a limited amount of gas and liquid phase remains in the larger β grains. The residual liquid phase primarily consists of heavier Eu-clusters due to their lower diffusion rate and follows the growth of the β grain lattice, subsequently exhibiting a hexagonal morphology akin to that

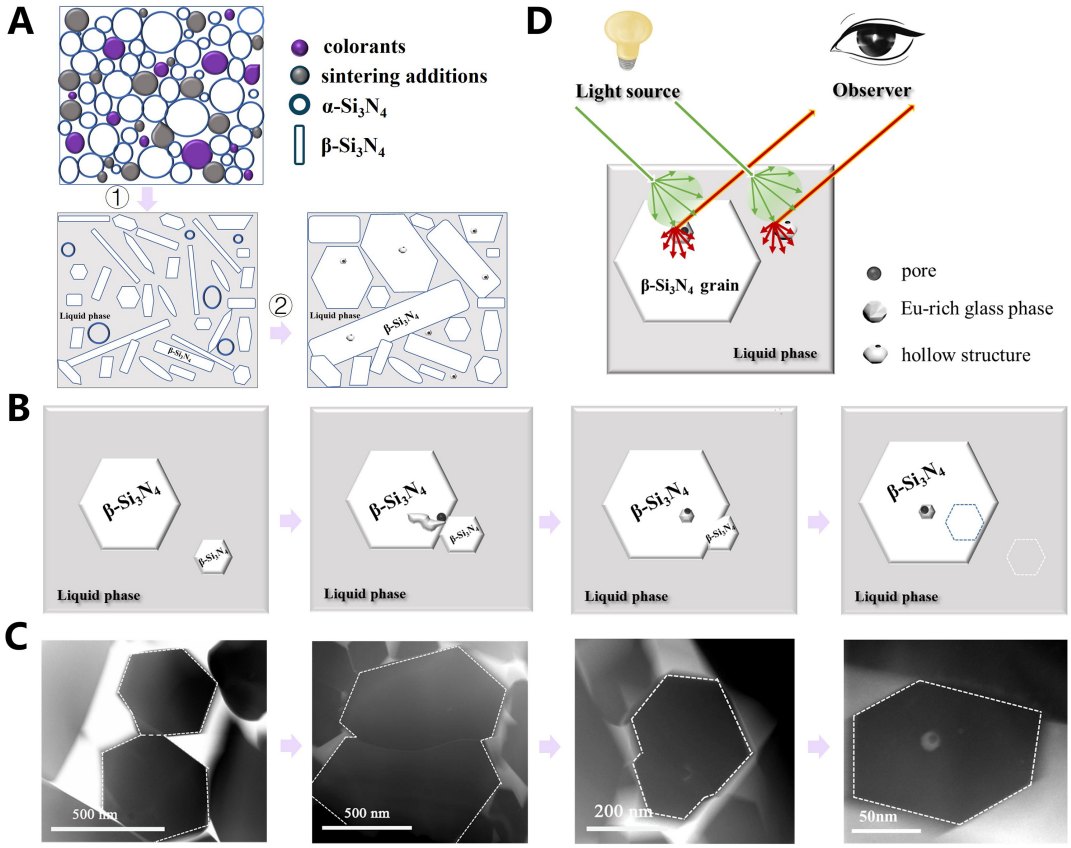


**Figure 1.** Schematic illustration. (A) The solution-reprecipitation process: firstly, α-$Si_3N_4$ powders, colorants and sintering additives are uniformly mixed; secondly, α-β phase transformation during liquid phase sintering; thirdly, the solution of small β grains and reprecipitation on large β grains, accompanying by the introduction of hollow structures into the large β grains. (B) The generation process of the hollow structures within grains. (C) Proofs for the formation process of the hollow structure in β grain under scanning transmission electron microscopy. (D) Light propagation path in $Si_3N_4$ ceramics (left) and the schematic illustration of the hollow structure (right).

of the β grain. In contrast, the residual gas is enveloped by the hexagonal liquid phase, forming a hollow structure. Figure 1D illustrates the coloring process for $Si_3N_4$ ceramics, wherein Eu ions within the hollow structures absorb blue-green light and emit red-orange light due to electronic transitions under photon excitation.

Samples with various $Eu_2O_3$ contents (2, 4, 5, 6, 7, 8, and 9 wt%) were designated as SEu-2, SEu-4, SEu-5, SEu-6, SEu-7, SEu-8, and SEu-9, respectively. SEM revealed that only rod-shaped grains and grain boundary liquid phases with distinct contrasts could be observed in the samples SEu-4, SEu-5, and SEu-6 [Supplementary Figure 4], aligning with prior research[32-34]. Interestingly, STEM detected the hollow structures ranging from ~5 to ~110 nm in both grains and grain boundaries, as depicted in Figure 2A-D and Supplementary Figures 5-7. Additionally, HRTEM analyses demonstrated that the hollow structure in β-grains exhibits a hexahedral morphology identical to that of the β-grains [Figure 2E-H and Supplementary Figure 7]. The corresponding Fast Fourier Transformation (FFT) patterns of region 1 [Figure 2E and Supplementary Figure 7G] and region 2 [Supplementary Figure 7H] suggest two hexagonal phases, but the lattice spacing, $d_{average}$ = 0.648, calculated from the FFT1 pattern, aligns with the zone axis [001], which falls in that of β-$Si_3N_4$ phase[35,36], whereas the lattice spacing, $d_{average}$ = 0.654, calculated from FFT2 pattern, is slightly different from that of the β grain. These findings suggest that the hollow structure is

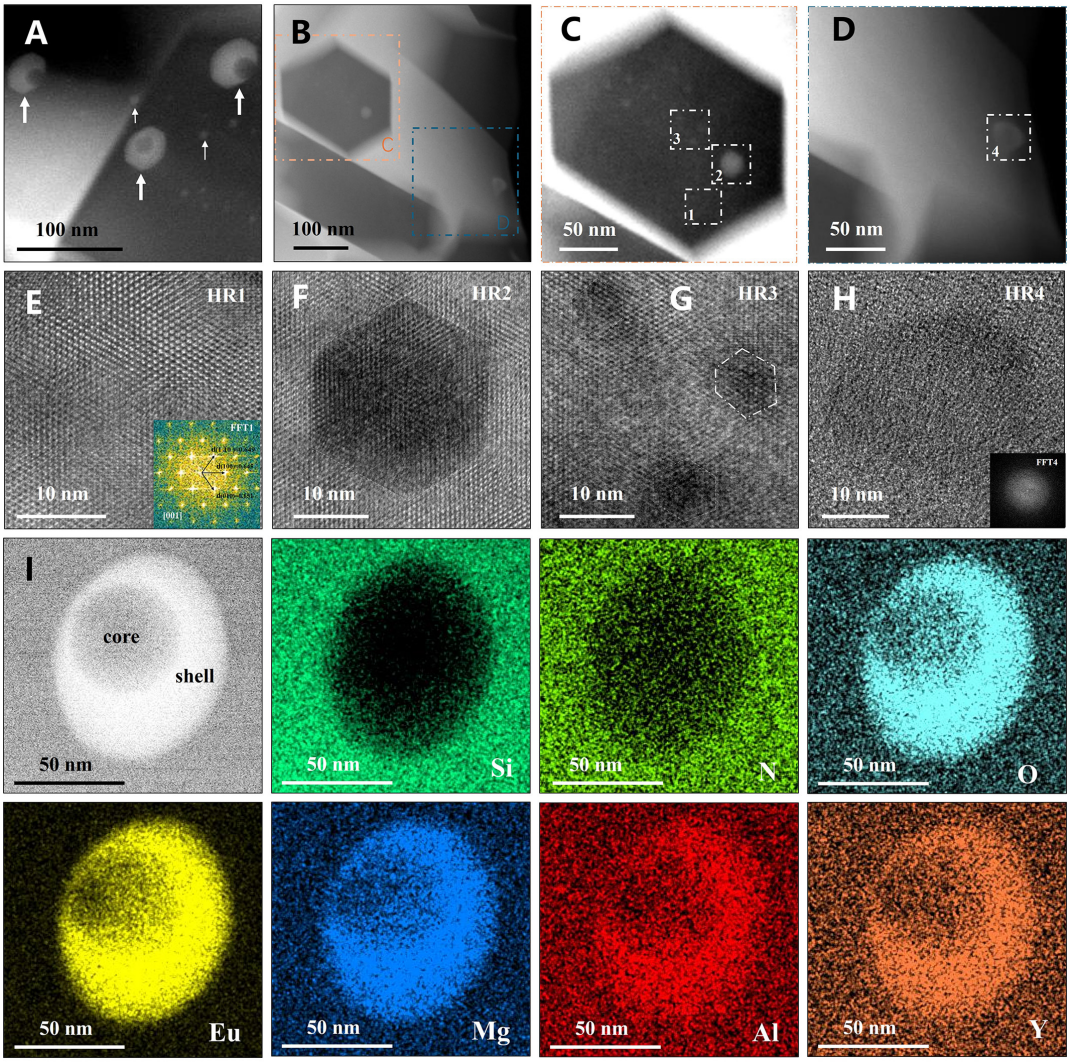


**Figure 2.** The crystallographic feature and chemical information of the hollow structure. (A and B) STEM images of the sample SEu-5 (the orange and blue squares mark the grain section and grain boundary regions, respectively): The hollow structures were formed in the grains and the grain boundary phase; (C) STEM magnified image of the orange area; (D) STEM magnified image of the blue area; (E-H) HRTEM images corresponding to the region 1-4 (the inset shows the corresponding FFT pattern). (I) STEM-EDS elemental analysis of hollow structure in sample SEu-5.

epitaxially grown on original β grains, albeit with minor distortions to the original crystal structure. Notably, the corresponding FFT4 pattern of the hollow structures at grain boundaries displays a halo indicative of an amorphous nature [Figure 2H], thus preventing the detection of the hollow structure by XRD patterns [Supplementary Figure 8] due to its amorphous nature. The chemical composition of the hollow structures is illustrated in Figure 2I and Supplementary Figure 9. Elemental maps reveal that the core, characterized by its element-free and rounded morphology, was classified as a pore. Conversely, the shell, which demonstrated a pronounced contrast difference with the β grains due to its enrichment in Eu elements, was identified as an Eu-rich secondary phase.

The electron valence states and luminescence of Eu ions in $Si_3N_4$ ceramics were examined using XPS, STEM-EELS, and SEM-CL techniques, as depicted in Figure 3A-C and Supplementary Figure 10. The XPS analysis of the SEu-5 sample revealed that both $Eu^{3+}$ and $Eu^{2+}$ signals, identified as $Eu^{3+}$:$3d_{5/2,3/2}$ and

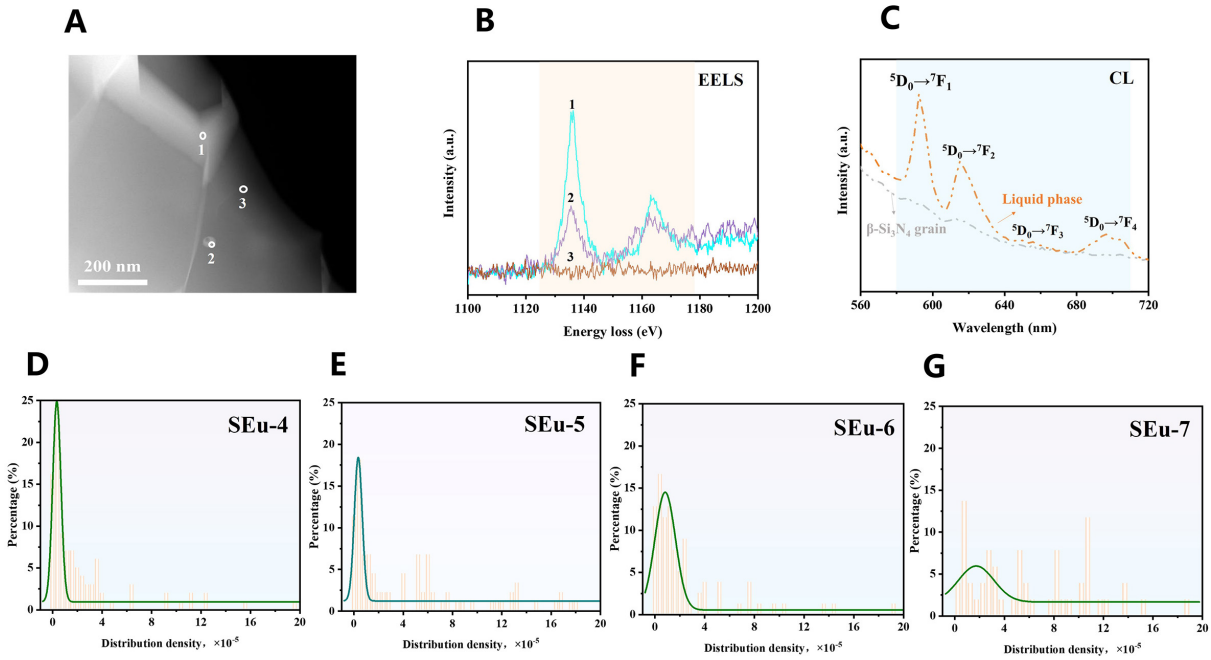


**Figure 3.** The valence states and luminescence of Eu ions. (A) STEM image of the sample SEu-5. (B) EELS spectra of the grain boundary phase (region 1), the hollow structure (region 2) and the β-$Si_3N_4$ grain (region 3) corresponding to the STEM image: The pairs of EELS signals at 1,135.8/1,164.0 eV attributed to the $Eu^{3+}$. (C) SEM-CL spectra of the β grain (grey line) and the grain boundary phase (orange line): There is a broadband emission peak at 530 nm and four narrow emission lines at 593, 616, 656 and 697 nm. (D-F) The distribution density of hollow structures in the sample SEu-4 (D), SEu-5 (E), SEu-6 (F) and SEu-7 (G) (the X-axis is defined as the average number of hollow structures per unit area ($nm^{-2}$); the percentage on the Y-axis refers to the relative frequency distributed in various hollow structure density intervals; the green lines mean Gauss Amp of the distribution density of hollow structure): With the increases of $Eu_2O_3$ content, the distribution density of hollow structure increases.

$Eu^{2+}$:$3d_{5/2,3/2}$, respectively, were readily found [Supplementary Figure 10]. This suggests a reduction of some $Eu^{3+}$ to $Eu^{2+}$ in an $N_2$ atmosphere. The STEM-EELS results indicated that the grain boundary glass phase (region 1) and the hollow structure (region 2) predominantly consisted of EELS signal pairs at 1,135.8/1,164.0 eV, attributed to $Eu^{3+}$[37], but no EELS peaks were observed in the β grains (region 3). The SEM-CL spectra of the β-grain and grain boundary phases in the SEu-5 displayed a broad emission peak and four narrow emission lines [Figure 3C]. The broad emission peak at 530 nm corresponds to the 5d-4f transition of $Eu^{2+}$. Additionally, several distinct lines at 593, 616, 656, and 697 nm are associated with the $^5D_0 \rightarrow ^7F_1$, $^5D_0 \rightarrow ^7F_2$, $^5D_0 \rightarrow ^7F_3$ and $^5D_0 \rightarrow ^7F_4$ transitions of $Eu^{3+}$[38,39], respectively. These CL emission peaks likely arise from the Eu-rich hollow structure present in grain boundary and β-grain. Consequently, the $Eu^{2+}/Eu^{3+}$-doped hollow structures present within grain boundaries and β-grains serve as a primary chromophore in $Si_3N_4$ ceramics. Furthermore, the distribution density of these hollow structures could be regulated via control of $Eu_2O_3$ content for color regulation of $Si_3N_4$ ceramics. The distribution density is defined as the average number of hollow structures per unit area ($nm^{-2}$) in the context of STEM, where 70 regions were randomly selected in each sample at magnification photography for counting. As shown in Figure 3D-G, the distribution density of the hollow structures progressively increases with $Eu_2O_3$ content. A higher distribution density implies more chromophores, leading to increased absorption of blue-green light. Further details will be explored in Figure 4.

The influence of hollow structures on the optical properties of $Si_3N_4$ ceramics was examined, as depicted in Figure 4. Yellow and orange $Si_3N_4$ ceramics were synthesized using varying $Eu_2O_3$ concentrations. As the $Eu_2O_3$ concentration escalated from 2 to 9 wt%, the color transitioned from yellow to orange-red, with a

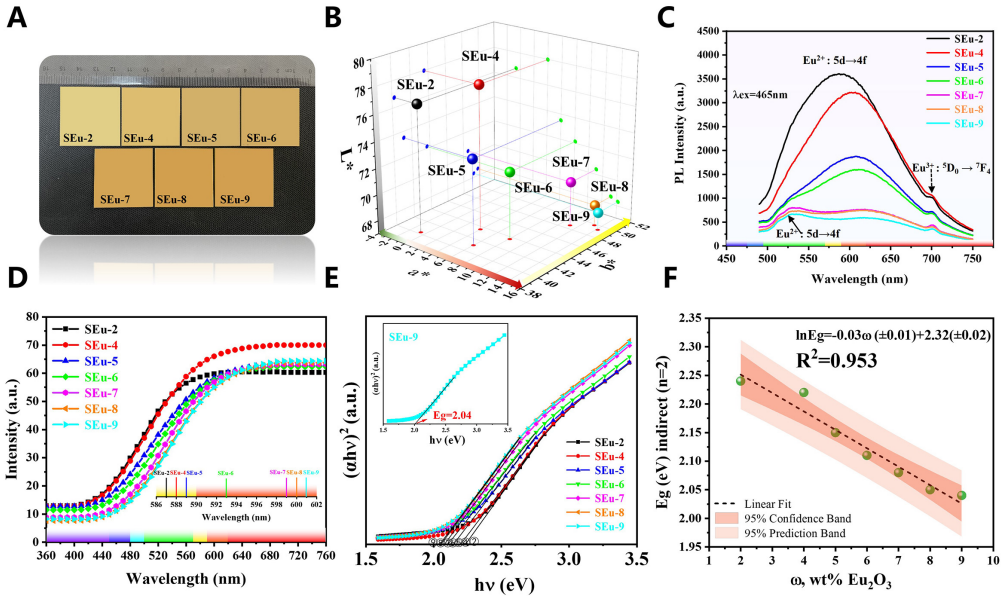


**Figure 4.** Color of $Si_3N_4$ ceramics. (A) Digital photo of $Si_3N_4$ ceramics with varying $Eu_2O_3$ mass rations: The orange color deepens with increasing $Eu_2O_3$ content. (B) L*, a* and b* parameters of Eu-doped $Si_3N_4$ ceramics: As the $Eu_2O_3$ content increases, the value of L* decreases, while the values of a* and b* increase. (C) Emission spectra of all samples by monitoring 465 nm excitation: As the $Eu_2O_3$ content increases, the emission spectra tend to redshift but the intensity of light emission is weakened. (D) Reflectance spectra of Eu-doped samples (the inset shows the reflected light of the samples is located in the wavelength range from 556 to 602 nm). (E) Plot of $(\alpha h\nu)^2$ *vs.* hν of Eu-doped $Si_3N_4$ ceramics (the insert shows the enlarged image of sample SEu-9). (F) Eg values for $Si_3N_4$ ceramics with different content of $Eu_2O_3$: An augmentation in the $Eu_2O_3$ content results in a reduction of Eg values, transitioning from 2.24 to 2.04.

heightened chroma [Figure 4A]. Figure 4B presents that the L* value diminishes while a* and b* values rise in response to the diminished brightness and a color shift towards reddish-yellow. The emission spectra of all samples by monitoring 465 nm excitation are shown in Figure 4C, where the intense broadband emission peaks for samples SEu-2, SEu-4, SEu-5, SEu-6, SEu-7, SEu-8, and SEu-9 occurred at 587, 605, 609, 612, 622, 624 and 626 nm, respectively, corresponding to the 5d→4f transition of $Eu^{2+}$[40]. A relatively faint yet broad emission is discernible at 530 nm, which can also be attributed to $Eu^{2+}$ ion emissions. A more pronounced narrow emission peak at 700 nm is evident later in the spectrum. The $^5D_0 \rightarrow {}^7F_4$ transitions of $Eu^{3+}$ ions account for this narrowband emission[39]. Additionally, samples SEu-2, SEu-4, SEu-5, SEu-6, SEu-7, SEu-8, and SEu-9 absorb blue or green light and exhibit strong reflectance in the yellow or orange wavelengths at 587, 588, 589, 593, 599, 600, and 601 nm, respectively [Figure 4D]. The band gap of Eu-doped $Si_3N_4$ ceramics falls within the yellow and orange light region (Eg: 2.03-2.4), as depicted in Figure 4E, and an increase in $Eu_2O_3$ content, a decrease from 2.24 to 2.04 in Eg values correspondingly [Figure 4F]. In conjunction with the findings presented in Figure 3D-G and the subsequent analysis of the optical properties of $Si_3N_4$ ceramics varying in $Eu_2O_3$ content, it can be deduced that the orange hue of $Si_3N_4$ ceramics exhibits a positive correlation with the distribution density of hollow structures. Specifically, as the distribution density of these structures increases, there is a corresponding rise in chromophore content. This leads to an enhanced absorption of blue-green light and a consequent increase in reflection of yellow-red light, resulting in a deeper orange coloration of the samples. Consequently, the coloration of $Si_3N_4$ ceramics can be effectively modulated by manipulating the distribution density of the hollow structures.

The impact of the hollow structures on the mechanical properties of $Si_3N_4$ ceramics was examined, as depicted in Figure 5 and Supplementary Figure 11. The $K_{IC}$ and σ initially increased, subsequently decreasing in line with the trend of relative density [Supplementary Figure 11]. The microstructures of the sample SEu-5, as revealed by SEM and TEM micrographs, exhibit elongated grains, grain pull-out, curved

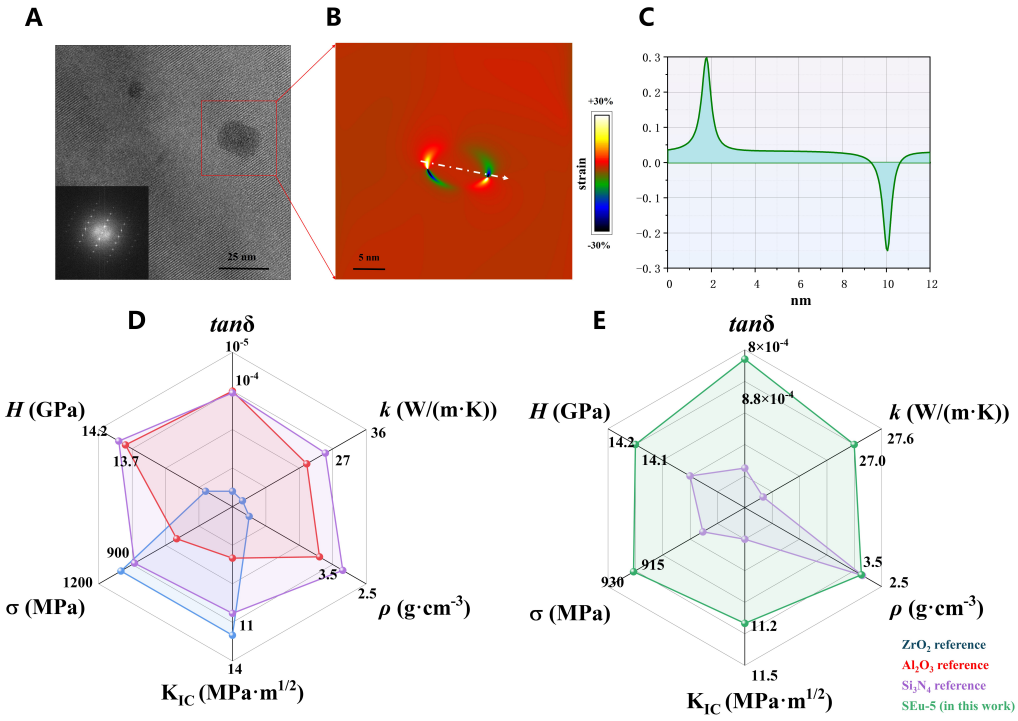


**Figure 5.** The strain distribution of the hollow structure and physical properties of $Si_3N_4$ ceramics. (A) HRTEM graph of the sample SEu-5 (the inset shows the corresponding FFT pattern). (B) Geometric Phase Analysis (GPA) mapping, derived from Digital Micrograph calculations, illustrates the overall strain field at a nanoscale. The color scale signifies the change in strain intensity, ranging from -30% (compressive) to +30% (tensile). (C) The profile of the white-dashed arrow in (B). (D) Physical performance of different ceramic materials with dielectric loss (tanδ), thermal conductivity (k), density (ρ), fracture toughness ($K_{IC}$), flexural strength (σ) and hardness (H) for referenced $ZrO_2$ ceramics, referenced $Al_2O_3$ ceramics and referenced $Si_3N_4$ ceramics plotted as a radar map: The performance of $Si_3N_4$ ceramics is outstanding. (E) Physical performance for referenced $Si_3N_4$ ceramics and the sample SEu-5: The sample SEu-5 exhibits better physical properties. The references for the physical properties of all ceramics in (D and E) are listed in the Supplementary Materials.

crack growth paths, and pronounced intergranular fracture [Supplementary Figures 12 and 13]. These attributes promote the utilization of crack energy and augment fracture resistance[41-44]. Consequently, the sample SEu-5 demonstrates superior mechanical properties, boasting a flexural strength of 915.5 ± 43.1 MPa and a fracture toughness of 11.1 ± 0.3 MPa·$m^{1/2}$ [Supplementary Figure 11]. The strain distribution depicted in Figure 5A is derived from geometric phase analysis (GPA), with the corresponding strain mapping illustrated in Figure 5B. Around the hollow structure, symmetrical compression-tension strain pairs are induced due to lattice mismatch [Figure 5C], which presumably leads to significant local internal stresses and a stress shielding effect[45], both of which contribute to enhanced friction resistance against motion or microcrack accumulation. Consequently, the strain couples associated with compressive-tensile forces surrounding hollow structures may present an additional avenue for improving the toughness of bulk ceramics. In this case, we evaluated the physical properties of reference $ZrO_2$ ceramics, $Al_2O_3$ ceramics, $Si_3N_4$ ceramics and the sample SEu-5. These properties included dielectric loss (tanδ), thermal conductivity (k), density (ρ), hardness (H), flexural strength (σ) and fracture toughness ($K_{IC}$) [Figure 5D and E, Supplementary Figure 1]. Our findings indicate that $Si_3N_4$ ceramics can compensate for the mechanical deficiencies of $Al_2O_3$ ceramics and the thermal and dielectric shortcomings of $ZrO_2$ ceramics, thereby exhibiting superior overall performance [Figure 5D]. In particular, the sample SEu-5 demonstrates superior physical properties compared to the referenced $Si_3N_4$ ceramics, with its tanδ, k, ρ, $K_{IC}$, σ, and H reaching 8.24 × $10^{-4}$, 27 W/(m·K), 3.24 g·$cm^{-3}$, 11.1 MPa·$m^{1/2}$, 915.5 MPa, and 14.1 GPa, respectively [Figure 5E]. The tanδ and ρ *of* the SEu-5 are ~100 and ~2 times lower than those of $ZrO_2$ ceramics, reducing signal

transmission absorbance and weight. The k of the SEu-5 is ~10 times higher than that of $ZrO_2$ ceramics, accelerating equipment cooling. The $K_{IC}$ and σ of the SEu-5 are ~2 times that of $Al_2O_3$ ceramics, enhancing damage tolerance and yield improvement.

## CONCLUSIONS

In summary, we introduce a microstructure design that involves the construction of Eu-doped hollow structures to synthesize $Si_3N_4$ ceramics. These ceramics exhibit a color transition from yellow to orange-red and possess superior mechanical properties. The hollow structure is characterized by its amorphous nature, with the core corresponding to the pore phase and the shell to the Eu-rich liquid phase. This structure functions as one of the dominant chromophores due to the 5d→4f transition of $Eu^{2+}$, which is coupled with the $^5D_0 \rightarrow {}^7F_J$ transition of $Eu^{3+}$ under photon excitation. Specially, the distribution density of this chromophore correlates positively with the depth of orange. Our sample, SEu-5, demonstrates optimized mechanical properties, with a flexural strength of 915.5 ± 43.1 MPa and a fracture toughness of 11.1 ± 0.3 $MPa{\cdot}m^{1/2}$. Factors such as grain pull-out, bridging and deflection, pronounced intergranular fractures, and the stress field surrounding the hollow structure collectively enhance the mechanical properties by reducing crack energy consumption.

## DECLARATIONS

### Acknowledgments

The authors would like to express their gratitude to Mr. Jingwei Feng for his invaluable support and guidance on the use of the transmission electron microscope.

### Authors' contributions

Conceiving the idea and designing the experiment: Liu N
Performing sample prep, data acquisition, and data analysis: Liu N, Hu T
Advising the scientific discussion on this research: Fu Z, Wang Z, Xu F, Dong S
Financial support: Duan Y
Supervising this research: Hu T, Zhang J
All authors participated in the writing of the manuscript.

### Availability of data and materials

Not applicable.

### Financial support and sponsorship

This work was supported by the National Natural Science Foundation of China (grant number: 52102082, Program Manager: Dr. Duan Y), Shanghai Science and Technology Committee (grant number: 21YF1454500, Program Manager: Dr. Duan Y), the State Key Laboratory of High Performance Ceramics and Superfine Microstructure of Shanghai Institute Ceramics, Chinese Academy of Sciences.

### Conflicts of interest

All authors declared that there are no conflicts of interest.

### Ethical approval and consent to participate

Not applicable.

### Consent for publication

Not applicable.

## REFERENCES

1. Basu B, Vitchev RG, Vleugels J, Celis JP, Van Der Biest O. Influence of humidity on the fretting wear of self-mated tetragonal zirconia ceramics. *Acta Mater* 2000;48:2461-71. DOI
2. Lv H, Bao J, Qi S, Jin Q, Guo W. Optical and mechanical properties of purple zirconia ceramics. *J Asian Ceram* 2019;7:306-11. DOI
3. Goeb O, Herrmann M, Siegel S. Thermodynamic and microstructural studies of coloration and decoloration processes during gas-pressure sintering of silicon nitride ceramics. *Key Eng Mater* 1998;161-3:217-20. DOI
4. Liu N, Zhang J, Duan Y, Li X, Dong S. Effect of rare earth oxides addition on the mechanical properties and coloration of silicon nitride ceramics. *J Eur Ceram Soc* 2020;40:1132-8. DOI
5. Yada M, Mihara M, Mouri S, Kuroki M, Kijima T. Rare earth (Er, Tm, Yb, Lu) oxide nanotubes templated by dodecylsulfate assemblies. *Adv Mater* 2002;14:309-13. DOI
6. Wang HQ, Batentschuk M, Osvet A, Pinna L, Brabec CJ. Rare-earth ion doped up-conversion materials for photovoltaic applications. *Adv Mater* 2011;23:2675-80. DOI PubMed
7. Carnall WT, Fields PR, Rajnak K. Spectral intensities of the trivalent lanthanides and actinides in solution. II. $Pm^{3+}$, $Sm^{3+}$, $Eu^{3+}$, $Gd^{3+}$, $Tb^{3+}$, $Dy^{3+}$, and $Ho^{3+}$. *J Chem Phys* 1968;49:4412-23. DOI
8. Carnall WT, Fields PR, Rajnak K. Electronic energy levels of the trivalent lanthanide aquo ions. IV. $Eu^{3+}$. *J Chem Phys* 1968;49:4450-5. DOI
9. Ren F, Ishida S, Takeuchi N. Color and vanadium valency in V-doped $ZrO_2$. *J Am Chem Soc* 1993;76:1825-31. DOI
10. Newman L, Lafleur WJ, Brousaides FJ, Ross AM. A spectrophotometric investigation of vanadium(V) species in alkaline solutions. *J Am Chem Soc* 1958;80:4491-5. DOI
11. Ocaña M, González-Elipe AR, Andrés-Vergés M, Tartaj P, Serna CJ, Orera VM. Preparation by hydrolysis of aerosols and colour properties of Cr-doped and Co-doped zircon powders. *J Eur Ceram Soc* 1998;18:821-30. DOI
12. Haubner R, Herrmann M, Lux B, et al. High performance non-oxide ceramics II. Berlin, Heidelberg: Springer; 2003.
13. Wu DN, Gong XY, Cui RR, Deng CY. Luminescence properties of $Ca^{2+}$ and $Si^{4+}$ co-doped strontium molybdate red phosphors for white LEDs. *J Mater Sci Mater Electron* 2016;27:9661-7. DOI
14. Vinothkumar G, Rengaraj S, Arunkumar P, Cha SW, Suresh Babu K. Ionic radii and concentration dependency of $RE^{3+}$ ($Eu^{3+}$, $Nd^{3+}$, $Pr^{3+}$, and $La^{3+}$)-doped cerium oxide nanoparticles for enhanced multienzyme-mimetic and hydroxyl radical scavenging activity. *J Phys Chem C* 2019;123:541-53. DOI
15. Cinibulk MK, Thomas G, Johnson SM. Fabrication and secondary-phase crystallization of rare-earth disilicate-silicon nitride ceramics. *J Am Ceram Soc* 1992;75:2037-43. DOI
16. Wang L, Qi Q, Cai P, et al. New route to improve the fracture toughness and flexural strength of $Si_3N_4$ ceramics by adding $FeSi_2$. *Scr Mater* 2017;126:11-4. DOI
17. Iizuka T, Hyuga H, Kita H, Osumi K. In situ synthesis of $Mo_5Si_3$ particle reinforced $Si_3N_4$ composite with crystallized grain boundary phase of $Yb_2Si_2O_7$. *Mater Sci Eng A* 2005;395:160-6. DOI
18. Ahmad S, Ludwig T, Herrmann M, Mahmoud M, Lippmann W, Seifert H. Phase evaluation during high temperature long heat treatments in the $Y_2O_3$-$Al_2O_3$-$SiO_2$ system. *J Eur Ceram Soc* 2014;34:3835-40. DOI
19. Murakami Y, Yamamoto H. Phase equilibria and properties of glasses in the $Al_2O_3$-$Yb_2O_3$-$SiO_2$ system. *J Ceram Soc Japan* 1993;101:1101-6. DOI
20. Richter HJ, Herrmann M, Hermel W. Calculation of heterogeneous phase equilibria in the system Si-Mg-N-O. *J Eur Ceram Soc* 1991;7:3-9. DOI
21. Zhang B, Zhuang H, Li W. Phase evolution of Y-α/β-sialon ceramic with YAG as a sintering additive. *J Mater Sci Lett* 2001;20:101-3. DOI
22. Santos C, Ribeiro S, Strecker K, Suzuki PA, Kycia S, Silva CRM. Crystallographic characterization of silicon nitride ceramics sintered with $Y_2O_3$-$Al_2O_3$ or $E_2O_3$-$Al_2O_3$ additions. *Ceram Int* 2009;35:289-93. DOI
23. Hayashi T, Munakata H, Suzuki H, Saito H. Pressureless sintering of $Si_3N_4$ with $Y_2O_3$ and $Al_2O_3$. *J Mater Sci* 1986;21:3501-8. DOI
24. Zhao DL, Zhang YJ, Gong HY, Nie LF, Zhao L. Effects of sintering aids on mechanical and dielectric properties of $Si_3N_4$ ceramics. *Mater Res Innov* 2010;14:338-41. DOI
25. Ikesue A, Furusato I, Kamata K. Fabrication of polycrystal line, transparent YAG ceramics by a solid-state reaction method. *J Am Ceram Soc* 1995;78:225-8. DOI
26. Ikesue A, Kinoshita T, Kamata K, Yoshida K. Fabrication and optical properties of high-performance polycrystalline Nd:YAG ceramics for solid-state lasers. *J Am Ceram Soc* 1995;78:1033-40. DOI
27. Tauc J, Grigorovici R, Vancu A. Optical properties and electronic structure of amorphous germanium. *Mater Res Bull* 1966;15:627-37. DOI
28. Tauc J, Menth A. States in the gap. *J Non Cryst Solids* 1972;8-10:569-85. DOI
29. Duan Y, Zhang K, Xie X. Electronic structural properties of β-$C_3N_4$, β-$Si_3N_4$ and β-$Ge_3N_4$. *Phys Status Solidi B* 1997;200:499-508. DOI

30. Yu B, Chen D. First-principles study on the electronic structure and phase transition of α-, β-and γ-$Si_3N_4$. *Acta Phys Sin* 2012;61:197102. DOI
31. Nogami M, Abe Y. Fluorescence spectroscopy of silicate glasses codoped with $Sm^{2+}$ and $Al^{3+}$ ions. *J Appl Phys* 1997;81:6351-6. DOI
32. Krstic Z, Krstic VD. Silicon nitride: the engineering material of the future. *J Mater Sci* 2012;47:535-52. DOI
33. Kleebe HJ, Pezzotti G, Ziegler G. Microstructure and fracture toughness of $Si_3N_4$ ceramics: combined roles of grain morphology and secondary phase chemistry. *J Am Ceram* 1999;82:1857-67. DOI
34. Liang YN, Lee SW, Park DS. Sliding behaviors of a unidirectionally oriented $Si_3N_4$W/$Si_3N_4$ composite. *Wear* 1999;224:202-10. DOI
35. Hardie D, Jack KH. Crystal structures of silicon nitride. *Nature* 1957;180:332-3. DOI
36. Lee MR, Russell SS, Arden JW, Pillinger CT. Nierite ($Si_3N_4$), a new mineral from ordinary and enstatite chondrites. *Meteoritics* 1995;30:387-98. DOI
37. Ponath P, Hamze AK, Posadas AB, et al. Surface structure analysis of Eu Zintl template on Ge(001). *Surf Sci* 2018;674:94-102. DOI
38. Krishnan R, Swart HC. Cathodoluminescence properties of monoclinic phased reddish-orange emitting $BaY_2(MoO_4)_4$:$Eu^{3+}$ phosphor. *Opt Mater* 2020;99:109604. DOI
39. Rakov N, Ramos FE, Hirata G, Xiao M. Strong photoluminescence and cathodoluminescence due to f-f transitions in $Eu^{3+}$ doped $Al_2O_3$ powders prepared by direct combustion synthesis and thin films deposited by laser ablation. *Appl Phys Lett* 2003;83:272-4. DOI
40. Qiao J, Xia Z. Design principles for achieving red emission in $Eu^{2+}$/$Eu^{3+}$ doped inorganic solids. *J Appl Phys* 2021;129:200903. DOI
41. Becher PF. Microstructural design of toughened ceramics. *J Am Ceram Soc* 1991;74:255-69. DOI
42. Hirosaki N, Okada A, Matoba K. Sintering of $Si_3N_4$ with the addition of rare-earth oxides. *J Am Ceram Soc* 1988;71:C-144-7. DOI
43. Mitomo M, Uenosono S. Microstructural development during gas-pressure sintering of α-silicon nitride. *J Am Ceram Soc* 1992;75:103-7. DOI
44. Kawashima T, Okamoto H, Yamamoto H, Kitamura A. Grain size dependence of the fracture toughness of silicon nitride ceramics. *J Ceram Soc Japan* 1991;99:320-3. DOI
45. Ding Q, Zhang Y, Chen X, et al. Tuning element distribution, structure and properties by composition in high-entropy alloys. *Nature* 2019;574:223-7. DOI